

RESEARCH PAPER

Impact of Synthesis pH on Nano-structural, Opto-electronic, and Photocatalytic Properties of TiO₂ Nanoparticles.

Dorah Kawira Muthee* and Birhanu Francis Dejene

Department of Physics, University of the Free State (QwaQwa campus) Private Bag, X13 Phuthaditjhaba, 9866, South Africa

ARTICLE INFO

Article History:

Received 12 October 2020

Accepted 29 February 2021

Published 01 April 2021

Keywords:

Anatase phase

Bandgap

Morphology

Photocatalysis

Sol-gel

ABSTRACT

TiO₂ is a wide bandgap semiconductor nanomaterial that has attracted considerable attention for its diverse applications. The structure, crystal size, morphology, and bandgap of TiO₂ play a vital role in photocatalysis and are related to the synthesis conditions and methods. In this study, the nanoparticles were synthesized using the sol-gel method and investigated the effect of varying pH on their structural and opto-electronic properties. The X-ray diffraction patterns revealed anatase phase in all the samples and presence of rutile phase (4wt%) at pH 7. The smallest crystal size was observed at pH 8, while a neutral pH gave larger crystal sizes. The TiO₂ grains were observed to have a nearly spherical spongy-like shape and agglomerated nanoparticles. The bandgap energy was found to increase with the increase pH value until neutral. The photocatalytic activity of the NPs was investigated by the degradation of methylene blue solution. The TiO₂ nanoparticles obtained at a pH of 8 exhibited the highest degradation efficiency of 82 % at a degradation rate of 0.0048/min.

How to cite this article

Kawira Muthee D and Francis Dejene B. Impact of Synthesis pH on Nano-structural, Opto-electronic, and Photocatalytic Properties of TiO₂ Nanoparticles.. J Nanostruct, 2021; 11(2): 305-316. DOI: 10.22052/JNS.2021.02.011

INTRODUCTION

With the rapid growth of industrialization, a significant amount of waste continues to be discharged into the environment. Despite clean water's value to society, these ongoing waste management systems appear to compromise water quality for everyday use. When dye contaminants from the cloth, food, leather, and paper industries, among others, are improperly disposed of, they pollute the atmosphere. The only way to deal with these dye contaminants is to establish safe disposal mechanisms and methodologies that will enable them to coexist with the ecosystem while maintaining a green environment. Photocatalysis is one technique used based on its eco-compatibility, energy

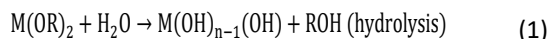
sustainability, and partial or total decomposition of the dye contaminants [1]. Photocatalysis is among the most promising environmental remediation approaches, and a tremendous amount of research work has been reported on several metal oxide-based nanomaterials [2]. TiO₂ semiconductor has unique properties and has been applied in diverse applications due to its chemical stability, low cost, mechanical robustness, strong oxidizing ability and efficient photocatalytic activity [3-6]. TiO₂ exists in nature under ambient temperature in three interconvertible polymorphs (brookite, rutile, anatase) [7, 8], and their properties are based on the type of polymorph. Besides, TiO₂ is an intrinsic N-type semiconductor due to oxygen vacancies generated during the heat treatment,

* Corresponding Author Email: kawirahdora@gmail.com

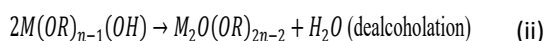
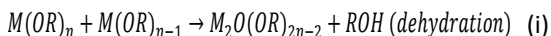


mainly when anatase composition is higher than that of other phases [9]. The anatase phase is the primary product in experimental synthesis, with a minor amount of either the brookite phase or rutile phase being formed. However, rutile is most thermodynamically stable among the metastable anatase and brookite phases [10].

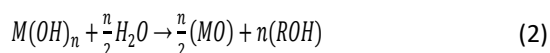
To prepare TiO₂ with the desired properties, different methods have been employed, such as hydrothermal [11], sol-gel [12], electrochemical [13], chemical vapor deposition [14], and hydrolytic precipitation [15, 16]. Amongst these methods, the sol-gel has been recognized as the most appropriate and straightforward chemical technique based on its versatility, low processing temperature, low-cost, stability, and high homogeneity [17]. Sol-gel involves the hydrolysis and condensation of the titanium alkoxides in aqueous media to produce different morphologies such as aerogels, wires, tubes, quantum dots, sheets, rods, and nanoparticles. In the presence of water, alkoxides are hydrolyzed and then polymerized to form a 3D oxide network as represented in Eq. (1) and (2) [18].



Condensation includes; dehydration (i) and dealcoholation (ii)



The overall equation



where R is alkyl group, M- Ti, Si etc. Water molecules in the overall equation (2) always bear a positive partial charge [19]. Thus, oxolation and Olation can proceed simultaneously during nucleation and growth, leading to TiO₂.nH₂O (amorphous hydrous oxide), where the number (n) of water molecules depends on experimental conditions. However, even with the study of synthesized TiO₂ nanoparticles (NPs), no clear and comprehensive understanding of the synthesis parameters that affect the structure, morphology, optical, and photocatalytic properties. The experimental procedure determines the precipitation of TiO₂ to form either anatase or

rutile [20]. When deoxolation (O = Ti-OH₂ → HO – Ti-Ti-OH) does not occur during nucleation, Olation leads to a linear growth along with one of the two equivalent directions in the equatorial plan of [TiO₂O₂(OH)₄(OH₂)₄]⁰ dimers. Then, Oxolation between the resulting TiO(OH)₂(OH)₂ linear chains after an internal proton transfer leads to corner-sharing octahedral chains (Ti₃O bridges) characteristics of the rutile structure. The formation of rutile may then be associated with the metastability of apical Ti=O bonds within monomers or dimers. If deoxolation occurs before Olation, condensation can continue along apical direction leading to skewed chains typical of the anatase structure. Controlling the stage of deoxolation before Olation can be obtained by adjusting the pH, which is one of the parameters that affect the final products of TiO₂.

Different structures and morphologies of titanium dioxide have been synthesized using different methods and pH values. For instance, Santhi et al. [20] synthesized nanorods at pH 7 and 9 while pure anatase phase was prepared by Anajafi et al. [21] at pH ranging from 8-12 using the hydrothermal method. Synthesis of mesoporous TiO₂ by Mutuma et al. [16] using a modified sol-gel method obtained a mixture of anatase-rutile phase at a pH of 2 and 9. Rod-like morphology was exhibited at pH 7 with a length ranging from 300–350 nm and a diameter of 70–100 nm, while at pH 9, the morphology changed from rod to nanoplatelet. Ismagilov et al. [22] deliberated the effect of nanoscale TiO₂ on cell responses by synthesizing four modifications of the TiO₂ (amorphous, anatase, brookite, and rutile) by varying the nature of precursor, pH, temperature, and addition of a complexing agent. The effect of pH (acid solution) on the structural, morphological, and optical properties of TiO₂ rutile nanorods was investigated by Selman et al. [23] for optoelectronic nanodevice applications. Moreover, the outcome observed at different pH is also determined by the solvents used. According to Sridevi et al., anatase-brookite phases were obtained at pH 6, 8, and 10, when 2- propanol solvent was used [24, 25].

The above research works show that pH plays a crucial role in the formation of TiO₂ NPs. Herein we report a reproducible one-step sol-gel method to synthesize TiO₂ nanoparticles. The reactions were carried out at acidic, neutral, and alkali pH (4, 6, 7, 8, and 10) to investigate the effect of pH on the

nano-structural and opto-electronic properties of the samples. The effect of how varied pH on the optical properties can affect the photocatalytic activity of TiO₂ NPs has not been widely explored. A comparison on photocatalytic activity was performed on the synthesized samples by degradation of methylene blue dye solution.

MATERIALS AND METHODS

Tetra isopropyl orthotitanate (C₁₂H₂₈O₄Ti) purity >98% purchased from Sigma Aldrich was used as titanium precursor, ethanol absolute (C₂H₆O), purity (>99.9%) as a solvent medium, ethanolamine as a stabilizer, and Deionized water to enhance the hydrolysis process. In contrast, ammonium hydroxide and hydrochloric acid were used for pH adjustment. All reagents were as received from the manufacturer.

TiO₂ synthesis procedure

TiO₂ sols were prepared by hydrolysis and condensation of Tetra isopropyl orthotitanate (TIP). 5 mL of TIP was dissolved in 20 mL of ethanol of spectroscopic grade with continuous stirring at room temperature, which was termed solution A. Ethanol was a preferred solvent since it has a lower dielectric constant (80) than water (24.3). Further, five different solutions were made with pH values varied as 4, 6, 7, 8, and 10 using ammonium hydroxide (18.1 M) and hydrochloric acid (12.1 M) and termed as solution B. Thereafter, solutions A and B were mixed under vigorous stirring using a Teflon-coated stirrer bar. After stirring the resultant solution for 30 min, 5 mL of ethanolamine was added dropwise, followed by a few drops of water to enhance the hydrolysis process, the sol was allowed to stir until the gel was formed. Following this procedure, the local precipitation effect was avoided. The gel was dried at 100 °C in a hot oven for 2 h to evaporate the residual solvents and water. Subsequently, the dried samples were annealed at 450 °C for 2 h in the air to crystallize the TiO₂ NPs [9]. The obtained products were crushed to a fine powder after cooling at ambient temperature, ready to be subjected for further characterization. The sol-gel method was adopted because it can synthesize a well-crystallized TiO₂ with anatase phase at very low temperature since TiO₂ formation is a water-driven process that occurs even at room temperature.

Characterizations

X-ray diffraction

The samples' structural analysis was done using Bruker AXS Discover diffractometer with CuKα (0.15406 nm) monochromatic radiation. The machine was set to scan at 40 mA and 40 kV in its reflective mode based on the Bragg–Brentano geometry conventional for powder samples. The powder samples were loaded on a Silicon low background sample holder and carefully placed on the XRD machine sample stage. The samples were scanned in the range of 20° ≤ 2θ ≤ 70° at a 2°/min scanning speed with a 0.02° fixed step size in 2θ. The crystalline phase's identity was justified based on the joint committee powder diffraction standard (JCPDS) from the International Centre for diffraction database. The average crystallite size (D) was estimated in comparison using the Scherrer equation (3) and Williamson-Hall (4) [20], the strain (4), dislocation density (δ) (5), Lattice parameters (tetragonal a = b, c) (6) below.

$$D = \frac{0.9\lambda}{\beta \cos\theta} \quad (3)$$

$$\beta \cos\theta = \frac{k\lambda}{D} + 4\epsilon \sin\theta \quad (4)$$

$$\delta = \frac{1}{D^2} \quad (5)$$

$$\frac{1}{d_{hkl}^2} = \frac{h^2+k^2}{a^2} + \frac{l^2}{c^2} \quad (6)$$

where 'λ' is the wavelength of CuKα radiation (1.54 Å), 'β' is the profile broadening, i.e., full width at half maxima (FWHM), in radians, while 'θ' is the Bragg's angle and where d_{hkl} is the spacing between the planes corresponding to h, k, l, miller indices calculated using Bragg's law.

Morphology/elemental studies

The surface morphologies and particle sizes of the synthesized samples were obtained using A Zeiss supro-field emission gun scanning electron microscope (SEM) and A JEOL 200CX high-resolution transmission electron microscopy (HRTEM, at an acceleration voltage of 200kV).

UV–VIS–DRS spectroscopy

The UV–VIS spectra of all samples were recorded by the Perkin Elmer Lambda 950 UV–Vis–NIR spectrophotometer fitted with Carry 100 software. The measurements were done with a

wavelength ranging from 250 to 800 nm equipped with an IRS 240 integrating sphere attachment. The spectra were recorded against the BaSO₄ reference.

Photoluminescence properties (PL)

The room temperature PL was done by the Cary Eclipse fluorescence spectrophotometer equipped with a 150 W xenon lamp as the excitation source and a grating to select a suitable wavelength for excitation. The grating slits were set at 10 nm for the excitation and 10 nm for the emission, while photomultiplier voltage was maintained at 500 mV. Each sample was loaded into a circular holder and excited with 315 nm radiation from the pulsed xenon lamp. The emission spectra were scanned in the range of wavelengths from 380 nm to 700 nm.

FTIR spectroscopic studies

To determine the nature and types of groups and their bonding, FTIR spectroscopy was characterized in the potassium bromide (KBr) phase using a Thermo-Scientific Nicolet FTIR Spectrometer attached to an automatic data acquisition center. Before measurement, KBr was dried at 80°C overnight. Transparent Pellets were made using a pellet press from finely grounded 0.001g of sample mixed with 0.2 g of KBr. A pure KBr pellet was also prepared in the same method and used as a reference spectrum. The measurement of the transmittance spectra was in the range 4000 cm⁻¹ to 400 cm⁻¹.

Photocatalytic evaluation.

This study was performed using the

Shimadzu-1700 UV-vis spectrophotometer to acquire MB absorption spectra from 200 to 800 nm. The experiments of the adsorption and photocatalytic performance of TiO₂ were performed using a 300 W xenon lamp for 150 min, and the temperature of the solution was maintained at 25°C throughout the experiment. 0.3g of the nanopowders were added to the 250 mL of methylene blue solution (12 ppm). The solution was magnetically stirred to ensure homogeneity. Before the light irradiation, the reaction system was stirred for 30 min in darkness to ensure the adsorption-desorption equilibrium. The suspension was irradiated under the UV light as a function of the irradiation time under constant stirring. Samples were taken at an interval of 15 min and centrifuged under 4000rpm for 2 min before measurements. Irradiation of MB without the photocatalyst was carried as the control for the experiment.

RESULTS AND DISCUSSION

Structural analysis

Fig. 1. (a) shows the XRD patterns of TiO₂ NPs samples prepared at various pH conditions. The peaks obtained at 2(theta) values 24.25°, 37.7°, 47.8°, 52.8°, 54.5°, 62.5°, 69.4°, 75.2° corresponds to (1 0 1), (0 0 4), (2 0 0), (1 0 5), (2 1 1), (2 0 4), (1 1 6), (2 2 0) crystal planes of the anatase TiO₂ phase (JCPDS card no.86-1157). The crystal structure of TiO₂ (anatase) is tetragonal with space group I4₁/amd with lattice parameters a = b = 3.7845 Å and c = 9.5143 Å. The prominent peak for all the prepared samples was observed at around 24.25°, corresponding to the (101) plane. 4 wt% amount of

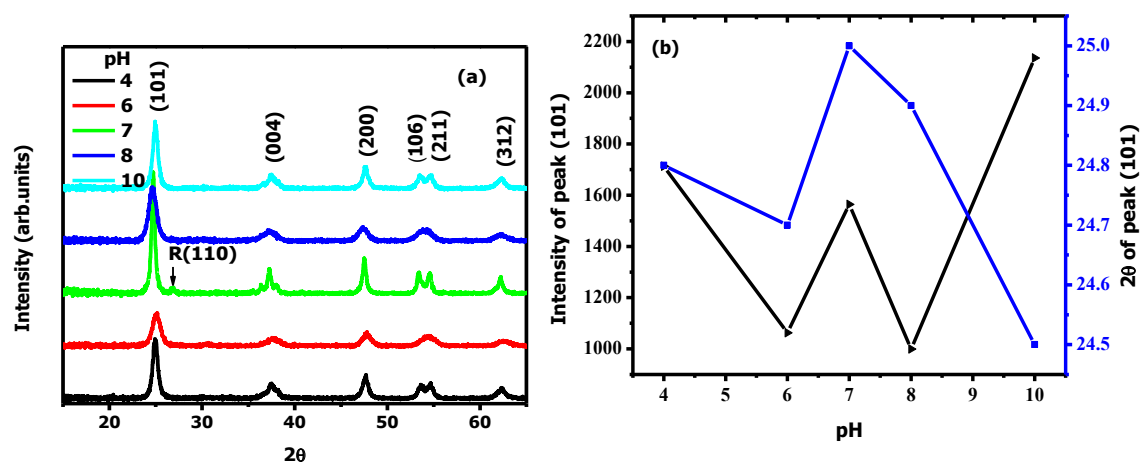


Fig. 1. (a) Representation of XRD patterns of samples prepared at various synthesis pH, (b) Depiction of a diffraction angle (2θ) with intensities of the peak (101) against synthesis pH for the TiO₂ nanopowders.

Table 1. The summary of calculated lattice parameters, crystalline sizes, dislocation density, and the strain of TiO₂ NPs obtained at different synthesis pH.

pH value	Crystal Size		dislocation	Lattice parameters		Cell volume	Strain (ε)
	Scherrer	W-H	density (δ × 10 ³)	a = b (Å)	c	(Å ³)	
4	26	74	1.479	3.719	9.637	133.29	0.0056
6	18	30	3.086	3.729	9.658	134.30	-0.0121
7	40	98	0.625	3.738	9.676	135.20	0.0040
8	16	25	3.906	3.743	9.685	135.69	-0.0055
10	26	63	1.479	3.754	9.697	136.65	0.0005

rutile phase was observed at pH 7, with a peak at 26.8° corresponding to (110) crystal planes (JCPDS # (86-0147). Rutile has a tetragonal structure with a space group of P4₂/mm and lattice parameter of a = b = 4.59330 Å and c = 2.95920 Å. The anatase to rutile transformation at neutral pH might have occurred during the titanium precursor hydrolysis, such that deoxygenation (O=Ti-OH₂) HO-Ti-Ti-OH conversion) did not happen. In this case, Olation can cause linear growth in the equatorial direction of the dimer [Ti₂O₂(OH)₄(OH₂)₄]⁰. This was followed by Oxolation between TiO(OH)₂(OH)₂ linear chains that lead to octahedral chains with corner-sharing, which is the characteristic of the rutile phase. The samples' peaks were strong and sharp evident to the samples' crystalline nature, while the intensities were found to vary non-uniformly according to Fig.1(b). The results in table 1, obtained by Scherrer equation and Williamson-Hall (W-H), suggested that the obtained crystallite size has an optimum pH value at neutral. In comparison, the average crystallite size values obtained by the Scherrer equation and W-H analysis showed considerable variation because the W-H plot considers the strain's effect. The crystalline sizes recorded for W-H were between 25 and 98 nm and agreed with Scherrer's equation, ranging between 16 and 40 nm crystallite size. The result from both methods indicated that the TiO₂ crystal structure is more crystallized at pH 7. According to table 1, the crystal sizes obtained at pH 6 and 8 suggested that weak acids and bases suppress crystal growth [24]. The strain caused in powders because of crystal imperfection and distortion in table 1 shows that the samples were experiencing expansive (positive) strain, while others had a compressive (negative) strain.

The crystallographic defects or irregularities

formed during crystal formation give rise to dislocations. The dislocation density (δ), tabulated in Table 1, is inversely proportional to the crystallite size of TiO₂ calculated from Scherrer's equation. The dislocation density decreased toward the neutral pH, which indicated that weak acids and alkali improve the crystallinity nature of the TiO₂ NPs. Lattice parameters (tetragonal a=b, c) [25, 26] were found to increase slightly, as displayed in Table 1, with increased synthesis pH and are somewhat lower than the lattice parameters from the reference file.

Morphology and composition analysis

SEM/EDS analysis

The morphology, crystallinity, and elemental composition of the synthesized samples were shown in Fig. 2. As observed in Fig. 2 (a-c), the images have nearly spherical spongy-like shapes, agglomerated nanoparticles and seem to be porous. When the pH was varied, the average particle sizes were around 25 nm and were larger than the crystallite sizes determined by Scherrer's equation, meaning that the particles observed in the SEM images are aggregated. There was no noticeable change in shape when the pH was increased. The sample prepared at pH 10 has the smallest grains, as seen in Fig.2(c), and Fig. 2(b) had larger grains that seemed to be uniformly distributed with good dispersion compared to (a) and (c). According to numerous studies, the variety of TiO₂ surface charges are pH-dependent. TiO₂ in sols possess an electric charge because of the absorption of H⁺ or OH⁻ in aqueous suspension [18]. The surface charge of TiO₂ can be determined by chemisorption of (iii) and (iv) :

For H⁺



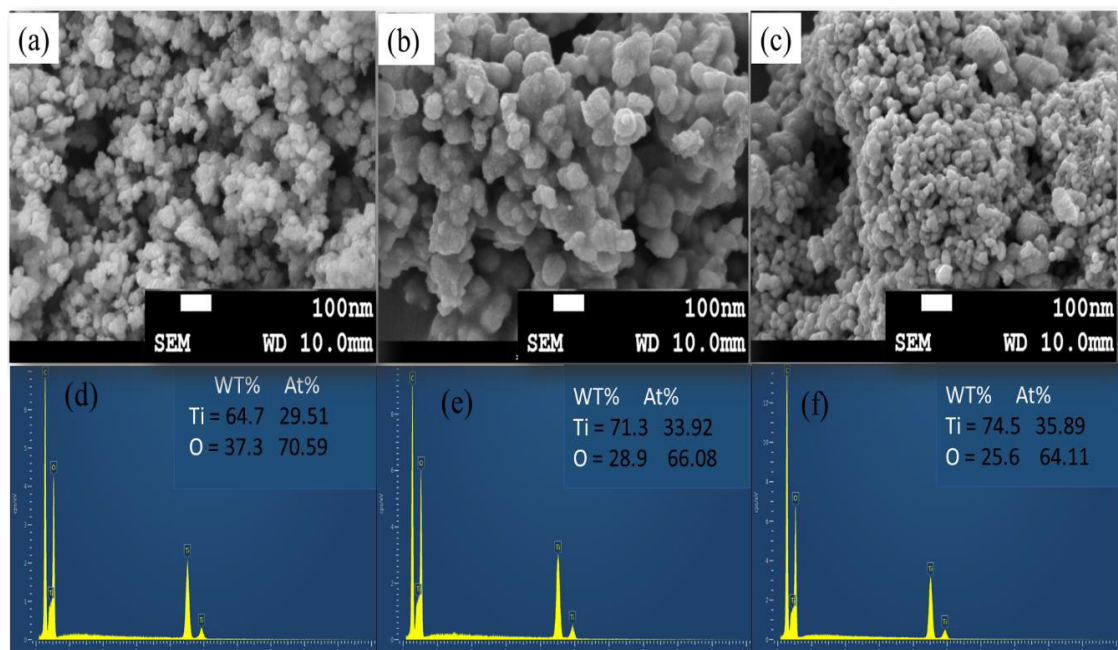
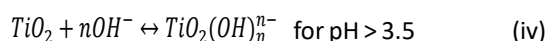


Fig. 2. SEM images for synthesis pH (a) 4, (b) 7, (c) 10 samples, and EDS spectrum for (a) 4, (b) 7, (c) 10 samples.

For OH⁻



The strong repulsive charge among particles in acidic and alkaline media reduces the likelihood of particle coalescence and allows for the formation of more stable sols. Growth of the grain sizes and morphology was probably controlled by the nucleation and growth methodology of TiO₂ NPs, which is identified with the pH in the TiO₂ integrated arrangement [27]. Studies by Su et al. [28] have indicated that the isoelectric of TiO₂ powder varies between the pH range 5-7. Based on this range, on account that samples 2(a) and (c) synthesized at pH of 4 and 10 are far from the scope of isoelectric factor, much fewer aggregates and smaller TiO₂ particles are formed. Our maximum particle size was at a pH of 7, which coincides with the isoelectric range of TiO₂. It is found that the morphology markedly depends on the synthesis pH.

The EDS results in Fig. 2 (d), (e), and (f) show that the synthesized samples are TiO₂ nanoparticles as confirmed by the presence of prominent peaks of Ti and O. These results confirm the XRD measurements on the absence of impurity element on the samples. The carbon traces observed are from carbon tape used during

the characterization. The elements' stoichiometric ratio was clearly understood by converting the weight to the compound's atomic percent. However, when the pH was increased, there was a slight change in the synthesized samples' chemical composition ratios. This change determines the variations observed in the morphology. Although the samples are slightly Ti-rich and O-poor, they are near the expected stoichiometric ratio of 1:2 of TiO₂ nanoparticles. This oxygen deficiency could lead to the defect-related blue emission in the PL analysis.

TEM/HRTEM analysis

The morphology, size, and structure of the prepared material were further illustrated using TEM, HRTEM, and SAED. The TEM images demonstrate that the synthesized samples are composed of nanosized, spherical-like particles confirming the SEM results. The image in Fig. 3(b) seems to have larger grain sizes than those in (a) and (c). The TEM images have an average particle size of $\approx 29 \pm 5$ nm. Further insight on the synthesized samples was gained by HRTEM measurements in Fig. 3(d) and (e). Fig. 3 (d) demonstrated a clear dispersion of the nanoparticles in the range of 24.5-31.0 nm. Besides, some agglomerations could be seen on the surface.

Fig. 3(e) shows that the lattice fringes and the

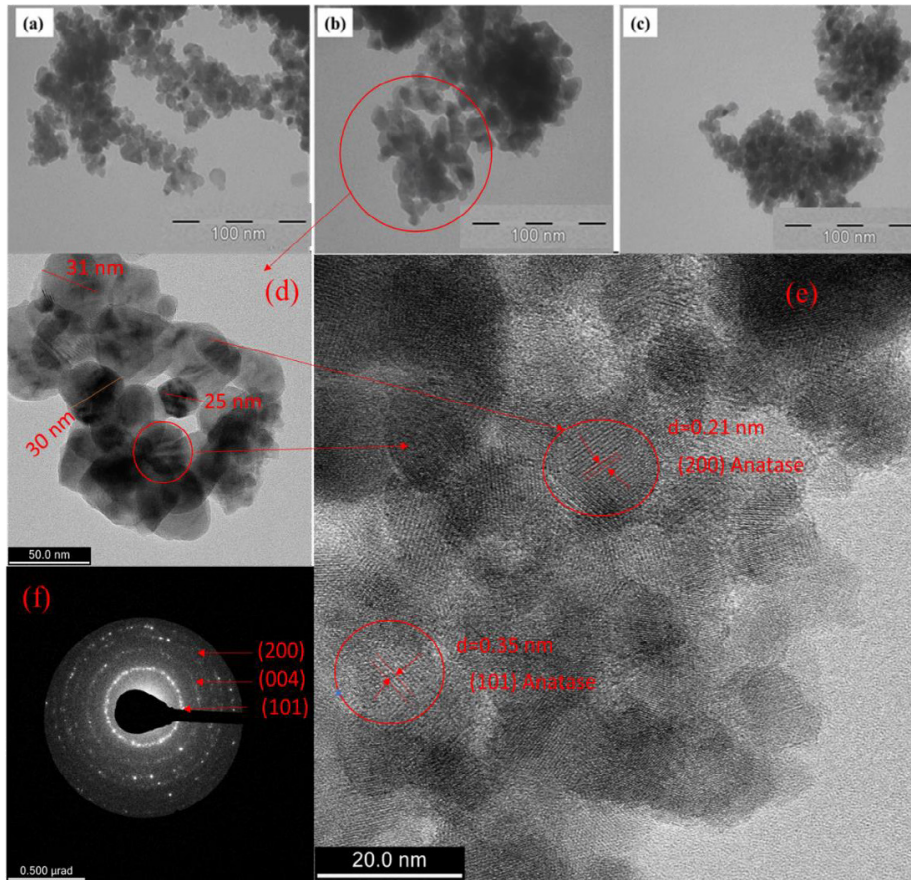


Fig. 3. TEM images for synthesis pH (a) 4, (b) 7 and (c) 10 samples, (d) and (e) HRTEM images of pH 7, (f) selected area diffraction (SAED) pattern at pH 7.

nanoparticle's lattice planes can be assigned from a distance. It shows that the fringes have a distinct spacing of 0.35 nm corresponding to the crystalline (101) plane of the anatase phase, which has the highest intensity in the XRD plot [29]. Fig. 2 (f) shows the SAED patterns of anatase TiO₂ at pH 7. It shows the apparent ring diffraction patterns with concentric circles of small spots indicating the material's polycrystalline nature and revealed the diffraction spots for TiO₂ anatase. The diffraction rings are indexed as (101), (004), and (200) planes confirming the formation of the tetragonal anatase phase, which is per the XRD results.

Optical and luminescence analysis UV-vis spectroscopy analysis

Fig. 4(a) shows the UV-vis diffuse reflectance (R) spectra of all the samples. The Kubelka Munk re-emission $F(R)$ [30] in Eq. (7) is proportional to the absorption co-efficient after eliminating the scattering effect was used to estimate the bandgap

of the samples.

$$F(R) = \frac{(1 - R)^2}{2R} \quad (7)$$

$F(R)$ versus wavelength plot for the TiO₂ nanoparticles was given in an inset of Fig. 4(a). It displayed a sharp absorption band around 400 nm, which was assigned to the optical bandgap due to electron transition from the valence to conduction band subtracting the exciton formation energy. A blueshift of the absorption edge is observed with an increase in pH values, indicating an increase in bandgap. The sample at pH 7 displayed the highest reflectance over the alternative samples due to its large crystal size and the induced oxygen vacancy (defect sites) [29]. A linear fit graph of $(F(R) hv)^2$ vs hv was plot to obtain the bandgap of the synthesized NPs, as shown in Fig.4(b). Where hv is the photon energy for each sample. The energy bandgap, E_g , was determined by extrapolating the linear section of the curve to

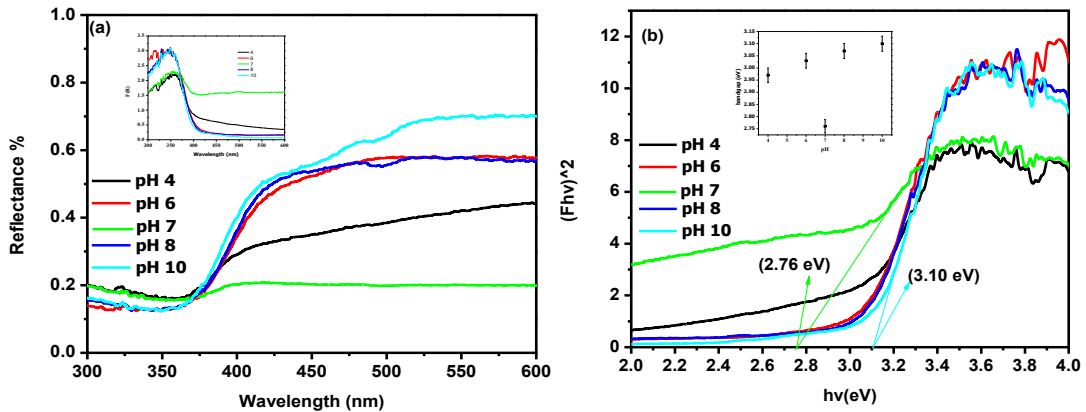


Fig. 4. (a) The diffuse reflectance spectra and (b) the bandgap for the TiO₂ nanoparticles prepared at various pH values.

the x-axis. At the x-intercept, [31]. It was evident from the plot an inset of Fig.4(b) that the bandgap values of the TiO₂ nanoparticles increased with an increase in pH. The rise in bandgap might be due to a decrease in crystallite size that determines the

quantum size effect, which causes the blue shift of the absorption edge in the diffuse reflectance [32, 33]. The bandgaps (range from 2.76 - 3.10 eV) are significantly less than the intrinsic bandgap of the bulk TiO₂ as given in the introduction (3.20 eV -

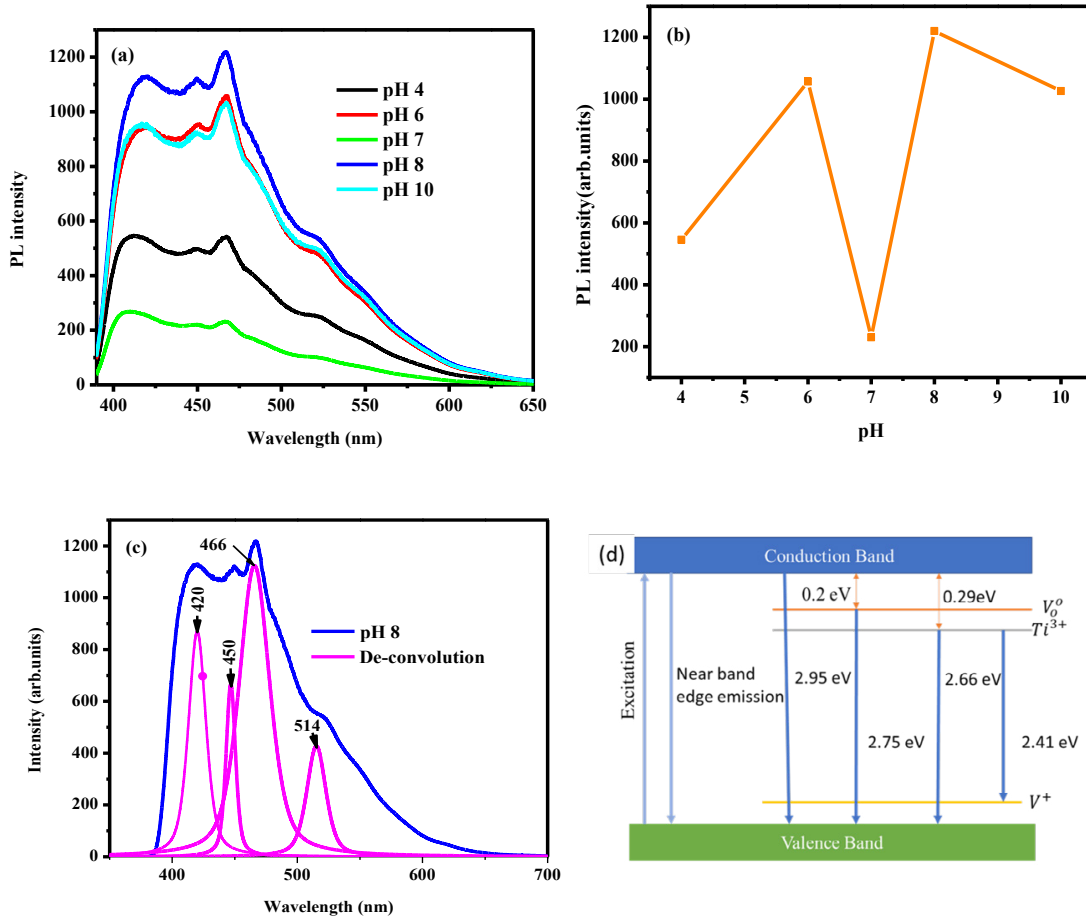


Fig. 5. (a) PL Emission spectra for TiO₂ NPs prepared at various synthesis pH, (b) Graph of pL intensities against the synthesis pH, (c) A deconvoluted graph of pH 8, (d) Schematic energy band diagram and the optical transitions in the TiO₂ nanoparticles.

anatase), signifying that the possible defect effects and exciton formation, play an essential role in the absorption.

Photoluminescence (PL) analysis

Photoluminescence (PL) emission spectra have been widely used to investigate the efficiency of charge carrier trapping, migration and to understand the state of electron-hole pairs in semiconductors. All Samples excited at a wavelength of 315 nm were shown in Fig:5 (a). Fig. 5(b) shows the PL intensities plot against the synthesis pH for the TiO₂ nanoparticles. The sample at neutral pH had the lowest PL intensity, ascribed to a high rate of non-radiative recombination and reduced number free charge carriers that can take part in pollutant degradation, hence decreasing the photocatalytic activity. All samples showed a broad emission band, which was deconvoluted using a Gaussian fit in Fig. 5c. From the deconvolution, four emission peaks were observed. The first emission peak located at 420 nm was attributed to a Self-trapped exciton localized on TiO₆ octahedra, which can be created by the direct recombination of a trapped electron in the lattice site with a hole or by the indirect recombination assisted by an oxygen vacancy [34]. The emission Peaks 450 and 466 nm were attributed to shallow traps close to the conduction

band edge, while the emission peak at 514 nm was ascribed to the deep trap state. The primary defects in TiO₂ are oxygen vacancies, which lead to the creation of Ti³⁺ centers. The electrons located on the oxygen vacancy state affect the electronic structure of TiO₂ by forming the donor level below the conduction band as shown in Fig:5(d) [34]. The defects are mainly located on the nanostructures' surface and could form a series of energy levels within the bandgap of TiO₂ by trapping electrons from the valence band.

FTIR analysis

FTIR technique allows the identification of the functional groups and chemicals present in the synthesized samples. Fig. 6 shows the FTIR spectra of the TiO₂ Synthesized by the sol-gel method, obtained in the range of 4000-400 cm⁻¹. The broad absorption band centered 3420 cm⁻¹ was assigned to hydroxyl groups' intermolecular interaction for water molecules with TiO₂ surface [35]. The peak observed at 1618 cm⁻¹ was characteristic of -OH of water's bending vibration mode associated with surface adsorbed water [36]. The band noticed at 1387 cm⁻¹ was assigned to the -CH₂, C-H, and -CH₃ stretching vibrations [37, 38]. Broadband with shoulder centered at 849 cm⁻¹ was assigned to the presence O-Ti-O stretching band, which is the characteristic peak of TiO₂ [39]. The sharpening

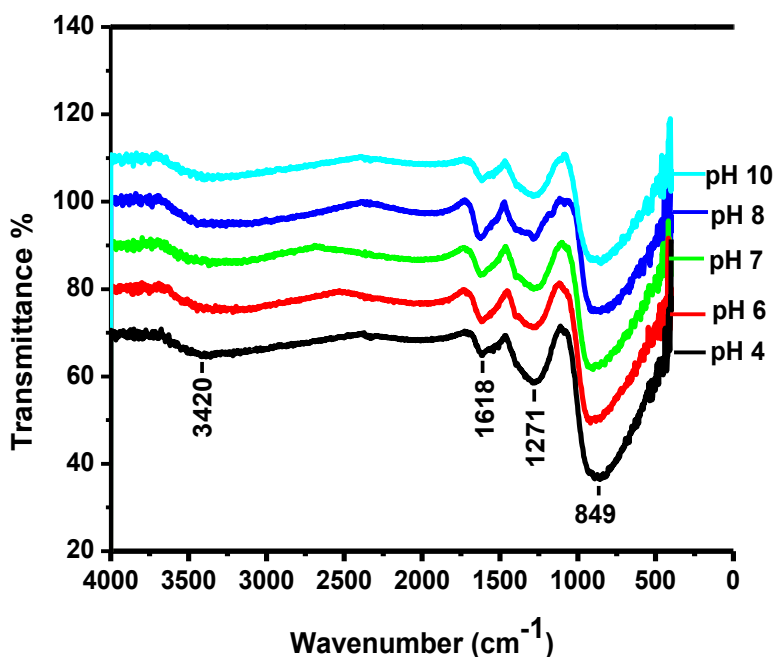


Fig. 6. FTIR spectra of the samples prepared at different pH values at region 4000-400 cm⁻¹

of the metal oxide's distinct peaks shows that the crystalline nature of TiO₂ increases with an increase in pH.

Photocatalysis

The samples' photocatalytic activity was investigated by the degradation of methylene blue (MB) dye under artificial UV light irradiation. Photocatalytic degradation is a complex process that involves at least interactive nanoparticles/semiconductors, water, and light [40]. The proposed photocatalytic process occurs when TiO₂ NPs are irradiated with electromagnetic radiation with energy equal to or greater than its bandgap. The absorption measurements were carried out to determine the degradation with respect to time. The absorption spectra' peak area is a direct measurement of the molecule concentration. Thus, its decrease with UV-irradiation time is a measure of the photocatalytic decomposition of the molecules. The degradation efficiency (%D) was obtained in relation to Beer-Lambert law according to Fig.7(a), which states that the concentration is directly proportional to the absorbance using Eq: (7) as follows;

$$\%D = \left(\frac{C_A - C_t}{C_A} \right) \times 100 \tag{8}$$

is the absorbance at time t = 0, and the is the absorbance at time (min) [41]. The MB photo-discoloration ratio was also calculated based on (Eq: 9) Langmuir-Hinshelwood model [42]. The model is established so that the only molecules degraded are those adsorbed by the catalyst, MB spinoffs are not measured, and the adsorbed molecules control the reaction rate.

Langmuir-Hinshelwood model can be stated as follows:

$$r = -\frac{dc}{dt} = \frac{kKC}{(1+KC)} \tag{9}$$

where r is the rate of degradation, C is the target pollutant concentration, t is the time (min), k is the rate constant of photodegradation reaction, and K is the absorption coefficient. When C is low, which is always the case for dyes (KC <<1), the reaction rate can be simplified to a pseudo-first-order kinetic model (Eq:10) with respect to the target dye concentration. K is estimated as the slope of the linear regression Versus t.

$$\ln \frac{C_A}{C_t} = kt \tag{10}$$

A high photocatalytic degradation rate corresponds to high photocatalytic activity. It shows that the degradation of MB strongly depends on the synthesis pH of TiO₂. The synthesis solution's initial pH determines the charge on the surface of TiO₂, and the adsorption of the pollutant on the catalyst surface is affected by these charges. Fig. 7 (a) shows MB's degradation efficiency for various pH values with respect to time. It was observed that %D was 60%, 39%,38%, 82%, and 71% for pH 4, 6, 7, 8 and 10 respectively. The degradation efficiency elevated with increasing initial pH in the range 4–8. Fig. 7 (b) displays a similar relationship as 7 (a). The data shows a good linear correlation, and the slopes calculated from the linear regression fit provided us with the value of the photocatalytic degradation reaction constants for each sample. It can be seen that the k constant improved from 0.026 min⁻¹ at pH 4 to

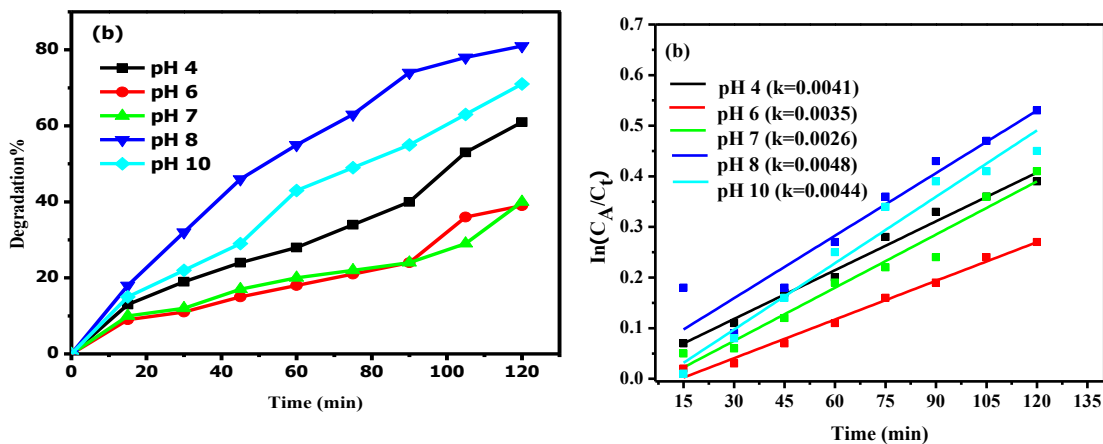


Fig. 7. (a) shows the rate of MB degradation at different irradiation time, (b) plot for Versus irradiation time.



0.048 min⁻¹ at pH 8. The high k constant acquired at high pH 8 might be because the high pH favors OH⁻'s formation through oxidation of OH⁻ by photo holes [43].

CONCLUSION

The TiO₂ NPs were prepared with varied synthesis pH by the sol-gel method. XRD confirmed that pH has a significant impact on the crystallinity and crystal size of TiO₂. The morphology of the different samples was not affected by pH, apart from the particle size. UV spectra showed that the bandgap of the synthesized TiO₂ NPs increased with an increase in pH value. It was observed that large crystal size leads to small surface area and therefore gives lower PL intensities. pH 8 was observed to have the highest degradation of 82% and decolorization rate of 0.0048/min after 120 min irradiation time. Therefore, longer electron-hole pair life would make the charge carriers contribute to the anatase phase's surface reaction. A lower electron-hole recombination rate is more desirable because increasing surface area adsorption of the reactants over the photocatalyst would increase the light absorption.

ACKNOWLEDGEMENTS

The authors wish to thank Dr. Bridget Mutuma for continued advice received during the work.

CONFLICT OF INTEREST

The authors declare that there are no conflicts of interest regarding the publication of this manuscript.

REFERENCES

1. Chen S, Xiao Y, Wang Y, Hu Z, Zhao H, Xie W. A Facile Approach to Prepare Black TiO₂ with Oxygen Vacancy for Enhancing Photocatalytic Activity. *Nanomaterials*. 2018;8(4):245.
2. Khan MM, Adil SF, Al-Mayouf A. Metal oxides as photocatalysts. *Journal of Saudi Chemical Society*. 2015;19(5):462-4.
3. Bai Y, Mora-Seró I, De Angelis F, Bisquert J, Wang P. Titanium Dioxide Nanomaterials for Photovoltaic Applications. *Chemical Reviews*. 2014;114(19):10095-130.
4. Fei Yin Z, Wu L, Gui Yang H, Hua Su Y. Recent progress in biomedical applications of titanium dioxide. *Physical Chemistry Chemical Physics*. 2013;15(14):4844.
5. Bianchi CL, Colombo E, Gatto S, Stucchi M, Cerrato G, Morandi S, et al. Photocatalytic degradation of dyes in water with micro-sized TiO₂ as powder or coated on porcelain-grès tiles. *Journal of Photochemistry and Photobiology A: Chemistry*. 2014;280:27-31.
6. Stucchi M, Bianchi CL, Pirola C, Vitali S, Cerrato G, Morandi S, et al. Surface decoration of commercial micro-sized TiO₂ by means of high energy ultrasound: A way to enhance its photocatalytic activity under visible light. *Applied Catalysis B: Environmental*. 2015;178:124-32.
7. Ramimoghdam D, Bagheri S, Abd Hamid SB. Biotemplated Synthesis of Anatase Titanium Dioxide Nanoparticles via Lignocellulosic Waste Material. *BioMed Research International*. 2014;2014:1-7.
8. Yan X, Li Y, Xia T. Black Titanium Dioxide Nanomaterials in Photocatalysis. *International Journal of Photoenergy*. 2017;2017:1-16.
9. Cavaleiro AA, Oliveira LCSd, Santos SALd. Structural Aspects of Anatase to Rutile Phase Transition in Titanium Dioxide Powders Elucidated by the Rietveld Method. *Titanium Dioxide: InTech*; 2017.
10. Vu NH, Le HV, Cao TM, Pham VV, Le HM, Nguyen-Manh D. Anatase-rutile phase transformation of titanium dioxide bulk material: a DFT +U approach. *Journal of Physics: Condensed Matter*. 2012;24(40):405501.
11. Yin H, Ding G, Gao B, Huang F, Xie X, Jiang M. Synthesis of ultrafine titanium dioxide nanowires using hydrothermal method. *Materials Research Bulletin*. 2012;47(11):3124-8.
12. Chen X, Mao SS. Titanium Dioxide Nanomaterials: Synthesis, Properties, Modifications, and Applications. *Chemical Reviews*. 2007;107(7):2891-959.
13. Anandgaonker P, Kulkarni G, Gaikwad S, Rajbhoj A. Synthesis of TiO₂ nanoparticles by electrochemical method and their antibacterial application. *Arabian Journal of Chemistry*. 2019;12(8):1815-22.
14. Nyamukamba P, Okoh O, Mungondori H, Taziwa R, Zinya S. Synthetic Methods for Titanium Dioxide Nanoparticles: A Review. *Titanium Dioxide - Material for a Sustainable Environment: InTech*; 2018.
15. Kalaivani T, Anilkumar P. Role of Temperature on the Phase Modification of TiO₂ Nanoparticles Synthesized by the Precipitation Method. *Silicon*. 2017;10(4):1679-86.
16. Idris A, Majidnia Z, Roushenas P, Nasiri R, Almaki JH. Anatase TiO₂ nanoparticles synthesis for removal heavy metals from wastewater International Science Postgraduate Conference 2014 Universiti Teknologi Malaysia 2014.
17. Phonkhokong T, Thongtem T, Thongtem S, Phuruangrat A, Promnopas W. Synthesis and characterization of TiO₂ nanopowders for fabrication of dye sensitized solar cells. *Digest Journal of Nanomaterials and Biostructures*. 2016;11:81 - 90.
18. Ibrahim SA, Sreekantan S. Effect of pH on TiO₂ Nanoparticles via Sol-Gel Method. *Advanced Materials Research*. 2010;173:184-9.
19. Ibrahim SA, Sreekantan S. Effect of pH on TiO₂ Nanoparticles via Sol-Gel Method. *Advanced Materials Research*. 2010;173:184-9.
20. Santhi K, Navaneethan M, Harish S, Ponnusamy S, Muthamizhchelvan C. Synthesis and characterization of TiO₂ nanorods by hydrothermal method with different pH conditions and their photocatalytic activity. *Applied Surface Science*. 2020;500:144058.
21. Anajafi Z, Marandi M, Taghavinia N. Hydrothermal synthesis of TiO₂ nanocrystals in different basic pHs and their applications in dye sensitized solar cells. *Physica E: Low-dimensional Systems and Nanostructures*. 2015;70:113-20.
22. Ismagilov ZR, Shikina NV, Mazurkova NA, Tsikoza LT, Tuzikov FV, Ushakov VA, et al. Synthesis of Nanoscale-

- TiO₂ and Study of the Effect of Their Crystal Structure on Single Cell Response. *The Scientific World Journal*. 2012;2012:1-14.
23. Selman AM, Hassan Z, Husham M. Structural and photoluminescence studies of rutile TiO₂ nanorods prepared by chemical bath deposition method on Si substrates at different pH values. *Measurement*. 2014;56:155-62.
 24. D. V S, K. T R, Jayakumar N, E S. pH dependent synthesis of TiO₂ nanoparticles exerts its effect on bacterial growth inhibition and osteoblasts proliferation. *AIP Advances*. 2020;10(9):095119.
 25. Tsega M, Dejene FB. Influence of acidic pH on the formulation of TiO₂ nanocrystalline powders with enhanced photoluminescence property. *Heliyon*. 2017;3(2):e00246.
 26. Chelbi S, Djouadi D, Chelouche A, Touam T. Structural and morphological properties of titanium dioxide-based sol-derived materials synthesized in different supercritical organic solvents. *Journal of Sol-Gel Science and Technology*. 2020;93(3):527-34.
 27. Abdulmajeed BA, Hamadullah S, Allawi FA. Synthesis and Characterization of Titanium Dioxide Nanoparticles under Different pH Conditions. *Journal of Engineering*. 2018;25(1):40-50.
 28. Su C, Hong BY, Tseng CM. Sol-gel preparation and photocatalysis of titanium dioxide. *Catalysis Today*. 2004;96(3):119-26.
 29. Yin H, Wang X, Wang L, N Q, Zhao H. Self-doped TiO₂ hierarchical hollow spheres with enhanced visible-light photocatalytic activity. *Journal of Alloys and Compounds*. 2015;640:68-74.
 30. Rahdar A, Aliahmad M, Azizi Y. NiO Nanoparticles Synthesis and Characterization. *Journal of Nanostructures*. 2015;5 145- 151.
 31. Motloung SV, Dejene FB, Ntwaeaborwa OM, Swart HC. Effects of catalyst/zinc mole fraction on ZnAl₂O₄:0.01% Cr³⁺ nanocrystals synthesized using sol-gel process. *Materials Research Express*. 2014;1(4):045029.
 32. Madhusudan Reddy K, Manorama SV, Ramachandra Reddy A. Bandgap studies on anatase titanium dioxide nanoparticles. *Materials Chemistry and Physics*. 2003;78(1):239-45.
 33. Molea A, Popescu V, Rowson NA, Dinescu AM. Influence of pH on the formulation of TiO₂ nano-crystalline powders with high photocatalytic activity. *Powder Technology*. 2014;253:22-8.
 34. Pan X, Yang M-Q, Fu X, Zhang N, Xu Y-J. Defective TiO₂ with oxygen vacancies: synthesis, properties and photocatalytic applications. *Nanoscale*. 2013;5(9):3601.
 35. Al-Taweel SS, Saud HR. New route for synthesis of pure anatase TiO₂ nanoparticles via ultrasound-assisted sol-gel method. *Journal of Chemical and Pharmaceutical Research*. 2016;8:620-626.
 36. Bagheri S, Shameli K, Abd Hamid SB. Synthesis and Characterization of Anatase Titanium Dioxide Nanoparticles Using Egg White Solution via Sol-Gel Method. *Journal of Chemistry*. 2013;2013:1-5.
 37. Hassan SM, Ahmed AI, Manna MA. Preparation and characterization of SnO₂ doped TiO₂ nanoparticles: Effect of phase changes on the photocatalytic and catalytic activity. *Journal of Science: Advanced Materials and Devices*. 2019;4(3):400-12.
 38. Al-Taweel SS, Saud HR, Kadhum AAH, Takriff MS. The influence of titanium dioxide nanofiller ratio on morphology and surface properties of TiO₂/chitosan nanocomposite. *Results in Physics*. 2019;13:102296.
 39. Muthee DK, Dejene BF. The effect of tetra isopropyl orthotitanate (TIP) concentration on structural, and luminescence properties of titanium dioxide nanoparticles prepared by sol-gel method. *Materials Science in Semiconductor Processing*. 2020;106:104783.
 40. Xu C, Rangaiah GP, Zhao XS. Photocatalytic Degradation of Methylene Blue by Titanium Dioxide: Experimental and Modeling Study. *Industrial & Engineering Chemistry Research*. 2014;53(38):14641-9.
 41. León ER, Rodríguez EL, Beas CR, Plascencia-Villa G, Palomares RAI. Study of Methylene Blue Degradation by Gold Nanoparticles Synthesized within Natural Zeolites. *Journal of Nanomaterials*. 2016;2016:1-10.
 42. Kumar KV, Porkodi K, Rocha F. Langmuir-Hinshelwood kinetics – A theoretical study. *Catalysis Communications*. 2008;9(1):82-4.
 43. Yang H, Deng J, Liu H, Yan W, Yang L, Yi B. Kinetics and mechanism of photocatalytic degradation of metobromuron by TiO₂ in simulated sunlight. *Research on Chemical Intermediates*. 2012;40(1):225-38.